Controlled Deposition and Glassification of Copper Nanoclusters

Hai-Ping Cheng and Uzi Landman*

School of Physics, Georgia Institute of Technology, Atlanta, Georgia 30332

Received: September 20, 1993

The dynamics and energy conversion and redistribution pathways in collisions of nanocrystals with bare solid surfaces and with adsorbed liquid films are investigated with molecular dynamics simulations. While impact of an ordered Cu_{147} icosahedral cluster on a bare Cu(111) surface at velocities larger than thermal leads to various outcomes including implantation, indentation, disordering, and spreading, deposition into a low-density liquid film (argon) results in efficient energy transfer to the liquid which for incidence velocities as high as 2–4 km/s can lead to controlled soft landing of a crystalline cluster on the solid substrate. For an incidence velocity of 2 km/s the cluster does not melt, maintaining its icosahedral structure, while for a velocity of 4 km/s the cluster superheats and melts and subsequently recrystallizes after soft landing on the Cu(111) surface. In collisions of the cluster with a higher-density liquid (xenon), with incidence velocities of 2–4 km/s, a larger fraction of the cluster translational energy is converted into internal energy of the cluster than in the case of the argon film. Such collisions lead to rapid attenuation of the cluster incident velocity, accompanied by ultrafast heating to high temperatures, superheating, and melting of the cluster. For certain impact velocities, e.g., 2 km/s into xenon, fast cooling via heat transport into the fluid can quench the metallic cluster into a glassy state. The branching ratios for conversion, partitioning, and dissipation of the incidence translational energy of the projectile cluster into internal degrees of freedom of the cluster and those of the target fluid are determined by the relative mass densities and sound velocities of the two materials. New methods for controlled growth of nanophase materials and for preparation of nanoglass aggregates, based on cluster deposition onto liquids, are suggested.

1. Introduction

Materials growth and the evolution of materials shapes, forms, and properties upon assemblage of small elementary units, or building blocks, to form larger aggregates are natural phenomena whose consequences we commonly observe. The elementary growth units may vary in size, from individual atoms and molecules[1] to small clusters,[2] nanoscale aggregates,[3] or larger size particles. Furthermore, the medium from which solid materials may be grown can be a homogeneous melt, or interphase interfaces such as a melt–solid interface as in liquid-phase epitaxy[4] or a gas–solid interface where epitaxial growth occurs via condensation of particles incident onto a solid substrate.[1,2] In the latter growth mode, which forms the basis for many modern materials fabrication techniques, particles may impinge onto a solid surface from the vapor or be deposited with a chosen incident energy via directed beams, as in atomic, molecular, or cluster beam epitaxy.[1,2]

Much of the research endeavor in this area is focused on the fundamental physical and chemical phenomena underlying growth phenomena, such as kinetics and dynamics of nucleation, equilibrium, and nonequilibrium properties of fluid–solid interfaces, phase transformations, collision dynamics and energy transfer and accommodation, heat and matter transport, sintering, and chemical reaction pathways.[5] Such basic understanding, often on a microscopic level, leads to identification of growth control parameters (GCPs) allowing controlled preparation of materials with desired structural, physical, mechanical, and chemical characteristics. Examples of GCPs include the nature of the deposited particles (atoms, molecules or clusters, in their ground or excited states) and deposition rates, incidence energy and direction, substrate temperature and cooling rates, substrate morphology, and stirring velocities.

Identification of the GCPs and their application in the development of novel materials preparation techniques are of great basic and technological significance, since correlations between physical and chemical properties of materials and their ultrafine microstructure and characteristic size are abundant among natural and human-fabricated materials. Such structure-property correlations have been long recognized and exploited;[3] examples include the human teeth material whose unique properties are related to its composition consisting of 1–2-nm fibrils of hydroxyapatite topotactically grown onto collagen, color enhancement achieved in ancient Egypt and China via reduction of the size of pigment particles through grinding or milling, and hardening of certain quenched metallic alloys discovered at the turn of the century, associated with the development of submicron precipitates of a new phase.

More recently, research efforts focus on methods of preparation and investigation of nanophase (also termed nanostructured) materials, that is, solids composed of nanoscale structural units which maintain their individual characteristics after consolidation. The interest in such materials is motivated by the new electronic, optical, magnetic, mechanical, and chemical properties which they exhibit.[3]

One of the main issues in the growing interdisciplinary area of nanophase materials is the controlled synthesis of solids with tailored size and shape distributions of the elementary nanoscale units. In this context we remark that the elementary units may be of crystalline or noncrystalline nature (in the latter case the assembled material is referred to as a nanoglass). Among currently used preparation techniques we note the accumulation of nanocrystals formed inside an evaporator onto a rotating cold finger and subsequent consolidation of the stripped-off powder, and sol–gel, organic "capping", and micellar techniques.[3]

In addition to the above materials-growth applications, controlled deposition of clusters onto targets is of importance for the preparation of well-characterized samples for investigations of clusters using physical probes. Examples include preparation of surface-supported clusters for studies with the use of tip-based (scanning-tunneling and atomic-force) microscopies[6] and deposition of clusters into solid inert matrices (matrix isolation) for

studies of vibrational and electronic structure of individual aggregates.

Guided by the above considerations, we reported recently[7] on theoretical investigations, using molecular dynamics (MD) simulations, of the energetics and dynamics of collisions of crystalline sodium chloride nanoclusters impinging onto fluid films adsorbed on sodium chloride solid surfaces.[8-10] Our results revealed the nature of energy conversion and redistribution pathways, involving crater formation in the liquid, vapor splashback, heating, melting, cooling, and generation of shock impulses, occurring when a nanocrystal impacts a fluid surface at hypervelocities. Furthermore, we found that the collision process and final state of the system can be controlled via appropriate choice of the liquid film for a given incident projectile. In our earlier studies we showed that a cubic-ordered nanocrystal of sodium chloride containing 64 atoms (($NaCl)_{32}$), incident with a center-of-mass velocity of 3 km/s (i.e., total translational energy of $\sim$87 eV) onto a 16-Å-thick adsorbed neon film, is "soft landed" onto the underlying solid substrate, preserving to a large degree its crystalline form and shape, while direct collisions of the cluster with a bare solid surface can lead to various outcomes including melting, disordering, fragmentation and rebounding of a vibrationally hot cluster, or fragments, from the surface. On the other hand, incidence of the same projectile onto a heavier mass adsorbed argon film of a similar thickness results in ultrafast heating and subsequent cooling (at rates of $\sim$10[15] and $\sim$10[14] K/s, respectively), occurring near the surface of the liquid film, leading to superheating followed by melting and quench of the cluster into a highly disordered, glassy state (the term "glass" refers here to a disordered solid formed by rapid cooling of the melt).

In the present study we investigate the collision dynamics of a metallic nanocluster, Cu_{147}, incident with various velocities onto adsorbed liquid argon and xenon films, as well as impinging on a bare Cu(111) surface. In section 2 we described the methodology for development of interatomic interaction potentials between rare-gas atoms and copper and provide pertinent details of our molecular dynamics simulations. In section 3 results of our simulations are presented, showing that deposition of a metallic Cu_{147} icosahedral cluster onto the lighter liquid film (argon) results in soft landing of the cluster for an incident velocity of 2 km/s and as high as 4 km/s (for the lower velocity the cluster does not melt maintaining an icosahedral structure, while for the higher velocity, upon collision the cluster heats up above its melting point and then soft lands and recrystallizes on the underlying Cu(111) surface). On the other hand, collisions of the cluster with a bare Cu(111) surface with these velocities result in damage to both the cluster and the target surface. Deposition of the cluster with an incidence velocity of 2 km/s onto a higher-density liquid (xenon) result in superheating followed by melting and rapid quenching into a glassy state. A detailed examination of the nature of the glassy cluster produced by this process is included. For higher incidence velocities the cluster superheats and melts, remaining as a hot liquid droplet for the duration of our simulations. (In our simulations the cooling rate of the droplet becomes exceedingly slow at the late stages because of the evaporation of the rare-gas atoms. It is likely that under appropriate conditions recrystallization of the cluster may occur.) We summarize our results in section 4, where we derive an expression relating the fraction of translational incidence energy of the projectile cluster which is converted into internal energy of the cluster, to characteristic physical properties of the cluster and substrate (target) materials (mass densities and sound velocities, or compressibilities).

These investigations suggest ways and means for size- and shape-controlled deposition of nanocrystals using inert fluids as buffers, as well as a novel method for ultrafast heating and cooling (orders of magnitude faster than the fastest cooling rates accomplished todate using sonochemistry techniques, 10[9] K/s, see ref 11a, and 10[10]–10[13] K/s achieved via the method of explosive spraying[11b], circumventing crystallization and producing nanoglass

particles. Our findings pertaining to glass formation of nanoscale metal particles are of particular interest due to the low propensity of metals (monocomponent, elemental systems, in particular) to glassify (that is, low "glass formability"[12-14]).

2. Interaction Potentials and Simulation Methodology

To investigate the atomic-scale dynamics and energy conversion and redistribution mechanisms in energetic collisions of a room-temperature Cu_{147} cluster with a bare Cu(111) surface and with adsorbed fluid argon or xenon films, chosen because of their chemically inert nature, we have used molecular dynamics (MD) simulations. In this method the Newtonian equations of motion of a system of interacting particles are integrated by a computer, yielding phase-space trajectories (particles' positions and momenta) and allowing exploration of the microscopic energetics, structure, and dynamics with refined resolution in space and time.[15,16]

The interatomic interactions in the copper substrate, in the Cu_{147} nanocluster, and between the copper surface and the cluster were modeled via the many-body potentials given by the embedded atom method (EAM).[17,18] The interatomic interactions between the rare-gas atoms (argon or xenon) were modeled using 6–12 Lennard Jones pair potentials with $\epsilon_{Ar} = 1.028 \times 10^{-2}$ eV, $\epsilon_{Xe} = 1.8913 \times 10^{-2}$ eV, $\sigma_{Ar} = 6.435$ au, and $\sigma_{Xe} = 4.45$ au[19] (the potentials were cutoff at a distance of 30 au).

2.1. Rare-Gas Interaction with Copper. Determination of interaction potentials between rare-gas atoms and metal surfaces has been the subject of a number of investigations, particularly in the context of rare-gase atom scattering from surfaces and the properties of physisorbed rare-gas films.[20-26] For our MD simulations, where the rare-gas atoms interact with both atoms of a solid copper surface and those of a copper cluster, we have developed additive pairwise interaction potentials which provide an adequate description of experimental data of Ar and Xe interaction with solid crystalline copper surfaces, as well as incorporating, by the method of construction, aspects of the interaction of the rare-gas atoms with copper atoms in different environments (such as in clusters).

For the pairwise interaction potential between a rare-gas atom and an atom of the metal at a distance r, we assume a form suggested and used in earlier studies[23,24] of rare-gas interactions with metal surfaces:

$$V(r) = V_0 e^{-\alpha r} - g(r,r_1) C_6 / r^6 \qquad (1)$$

with V_0, α, r_1, and C_6 as parameters to be specified below, and g is a damping function[23] of the form[25]

$$g(r,r_1) = e^{-(r_1/r-1)^2} \qquad \text{for } r \leq r_1 \qquad (2a)$$

$$g(r,r_1) = 1 \qquad \text{for } r \geq r_1 \qquad (2b)$$

The first term in eq 1 describes electrostatic repulsion due to charge-density overlap and Pauli exclusion and the second term corresponds to attraction due to dispersion interactions. To fit the parameters of the potential given in eq 1, we performed calculations of the interaction between individual Ar and Xe atoms and a Cu atom, using the local-spin-density-functional (LSD) method, employing a linear combination of atomic orbitals (LCAO) and a discrete variational method (LSD-LCAO-DVM),[27] together with a fitting procedure guided by an empirical data base for rare gas/metal surface systems.[22]

The LSD-LCAO-DVM method provides a proper description of the shape of the atom–atom interaction potential and rather accurate values for the equilibrium interatomic distances and vibrational frequencies. However, as is the case with all methods using the local-density-functional approximation, the calculated binding energies are overestimated. Moreover, long-range dispersion (van der Waals) interactions cannot be determined with this method. Plots of calculated energy versus interatomic distance for Cu–Ar and Cu–Xe are shown in Figure 1.
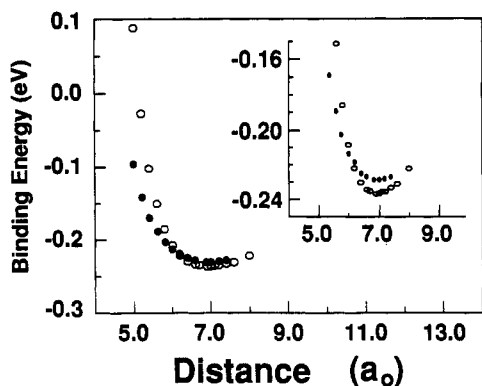
Figure 1. Binding energy versus interactomic distance for Xe–Cu (empty circles) and Ar–Cu (filled circles) calculated via the LSD-LCAO-DVM method. The interatomic binding energy curves near the minimum are shown on a larger scale in the inset. Energies in electronvolts and distances in Bohr radii (a_0).

The two experimentally estimated values which we use to guide our fitting procedure are the coefficient C_3 of the long-range interaction, $-C_3/r^3$, between the rare gas and a clean Cu(111) surface determined from calorimetric measurements, and the value of the atom to surface binding energy E_b obtained from desorption experiments. (We should note the large uncertainty in the values quoted in the literature[22] for characteristic parameters of the Ar/Cu(111) and Xe/Cu(111) systems.)

The fitting procedure consists of calculations of the interaction of the rare-gas atom with the Cu(111) surface, using eq 1 for the pairwise interactions with a starting value of C_6 obtained from the relation $C_6 = C_3 d^3(6/\pi)$, where d is the interlayer spacing in the surface, and C_3 estimated from the experimental data,[22] and the parameters V_0, α, and r_1 determined via a least-squares fit to the calculated interatomic energy curves (see Figure 1), including an overall energy shift E_0. Starting from an initial guess for E_0 the atom–surface interaction energies were calculated as a function of the height of the rare-gas atom above the surface for several adsorption sites in the Cu(111) surface. This procedure was repeated for a mesh of values of E_0 (and for each value a new set of parameters V_0, α, and r_1 and slight variations in the value of the C_6 coefficient) until a value for the binding energy E_b in the optimal adsorption geometry (i.e., the rare-gas atom adsorbed over the hollow site of the Cu(111) surface unit cell close to the experimentally estimated value was obtained. The optimized interatomic interaction potentials, $V(r)$, and atom-to-surface interactions for Ar–Cu(111) and Xe–Cu(111), plotted versus height above the hollow site and for the on-top adsorption site, are shown in Figure 2. The optimal values of the interatomic interaction potential parameters (eq 1) determined by the above procedure are given in Table 1.

2.2. Molecular Dynamics Simulations. In our simulations the calculational cell of the crystalline Cu(111) surface consisted of n_d layers of dynamic particles ($n_d = 12$ for calculations involving a bare Cu(111) surface and $n_d = 4$ for simulations of collisions with adsorbed films) with 400 atoms/layer arranged in a fcc crystalline structure and exposing the (111) surface. These layers were positioned on top of six layers of a static copper crystal of the same crystallographic orientation. For simulations involving adsorbed films the system was prepared with a fluid film (argon or xenon) equilibrated on top of the crystalline surface (the thicknesses of the liquid films were ~120 a_0 for argon and ~170 a_0 for xenon). The substrate calculational cell was repeated periodically in the two directions parallel to the (111) surface plane, with no boundary conditions applied in the normal (z) direction.

The target surfaces were initially equilibrated at the desired temperature (84, 84, and 161 K for the bare Cu(111) surface or with an adsorbed film of argon or xenon, respectively). During subsequent simulations of the collisions of clusters with the surface the temperature was controlled via application of stochastic
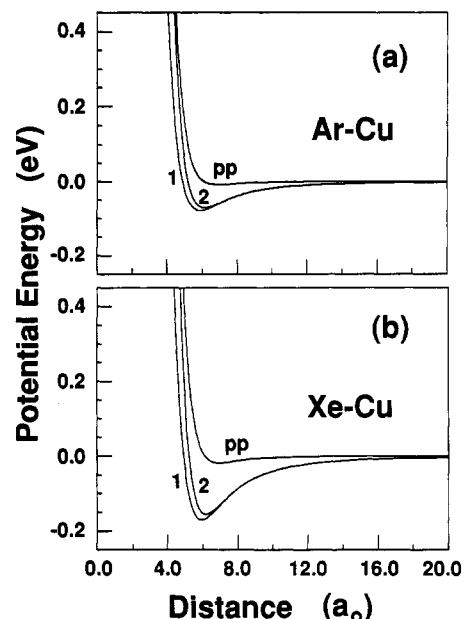

Figure 2. Optimized interatomic pair potentials (PP) for Ar–Cu and Xe–Cu, plotted versus interatomic distance, and rare-gas atom interaction potentials with the Cu(111) surface, for Ar/Cu(111) (in a) and Xe/Cu(111) (in b) plotted versus height (distance along the normal to the surface) of the rare-gas atom above the hollow adsorption site (marked 1) and for the on-top site (marked 2). The difference between the minima for the two sites, representing the surface corrugation of the interaction potential, is 7 meV for Ar/Cu(111) and 15.4 meV for Xe/Cu(111). Energies and distances in units of electronvolts and Bohr radii, respectively.

TABLE 1: Values for the Parameters of the Optimized Interatomic Pair Potentials, of the Form Given in Eqs 1 and 2, for Ar–Cu and Xe–Cu, with Interatomic Distances in a_0 and Energies in electronvolts[a]

	V_0 (eV)	$\alpha(a_0^{-1})$	C_6 (eV a_0^6)	r_1 (a_0)
Ar/Cu	2799.6	1.8809	1600	8.3
Xe/Cr	5866.1	1.8931	3500	8.0

[a] Using the parameters given in the table, the calculated values for Ar/Cu(111) for the C_3 coefficient of the long-range dispersion term and for the binding energy E_b are C_3(Ar) = 1583 meV Å[3], E_b(Ar) = 78.17 meV at a height z_m = 3.1 Å above the hollow adsorption site and 71.16 meV at z_m = 3.25 Å above the on-tope site. These values compare well with experimentally estimated ones,[22] C_3(Ar) ~ 1550 meV Å[3] and E_b ~ 80 meV. The calculated values for the Xe/Cu(111) system are C_3(Xe) = 3461 meV Å[3], E_b(Xe) = 170.7 meV at a height z_m = 3.1 Å above the hollow adsorption site, and 155.3 meV at z_m = 3.25 Å above the on-top site, compared with the experimentally estimated ones[22] of C_3(Xe) ~ 3150 meV Å[3] and E_b ~ 180 meV.

thermalization,[28] at the appropriate temperature, to the bottom dynamic layer of the solid surface region, with a stochastic collision frequency of 5 × 10⁻³ fs⁻¹. The equations of motion were integrated using the fifth-order Gear algorithm[15] with a time step Δt = 2–3 fs, which ensures conservation of energy throughout the collision process.

Finite clusters exhibit various structural isomers, depending on their internal vibrational temperature, with the structural motiffs dependent on the cluster composition and size. Moreover certain cluster sizes (termed "magic numbers") are more stable than others and consequently are more abundant. For metals (such as nickel[29]) it is expected that for clusters with up to 2000 atoms the lowest energy structures are of icosahedral symmetry, with magic numbers 13, 55, 147, ... In our simulations we have chosen a 147-atom icosahedral cluster, Cu₁₄₇, initially equilibrated at 300 K.

After equilibration of the separated collision partners, a velocity $V_c^{cm}(0)$ was assigned to the cluster atoms in the normal direction of incidence onto the surface and the collision process was simulated. The numerically generated dynamical phase-space trajectories and several other properties were recorded and
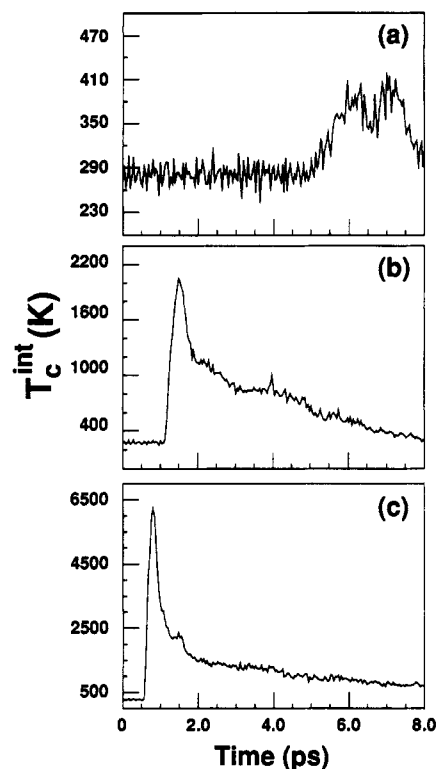
Figure 3. Variation of the internal temperature, T_c^{int}, of a Cu_{147} icosahedral cluster, equilibrated initially at a temperature of 300 K, plotted versus time during collisions with a cold (84 K) Cu(111) surface. Results are shown for incidence velocities of 0.023 km/s (i.e., thermal velocity, in a), 2 km/s (in b) and 4 km/s (in c). Temperature in degrees kelvin, and time in picoseconds.

analyzed. In discussing the energetics of the cluster, it is instructive to distinguish a kinetic energy component representing overall (center-of-mass) motion (K_c^{cm}) from an internal kinetic energy ($E_{k,c}^{int}$) component corresponding to particle "thermal" motion. We take $E_{k,c}^{int}$ to be the kinetic energy in a coordinate system comoving with the cluster's center of mass. In equilibrium steady-state conditions equipartition of energy between the various degrees of freedom results in a direct relation between the internal temperature (or temperature for short) of a set of N particles and the average of E_k^{int} ($3Nk_BT/2 = \langle E_k^{int} \rangle$, where k_B is the Boltzman constant). While we do not expect that full equilibrium conditions will be achieved throughout most of the initial collision processes, we often express the internal kinetic energy of a set of particles as their kinetic temperature.

3. Results

3.1. Collisions with a Bare Cu(111) Surface. Prior to discussion of our results for deposition onto liquid films, which are the main subject of this study, we remark on collisions between a room temperature Cu_{147} cluster with a cold ($T = 84$) bare Cu(111) surface, for various incident velocities $V_c^{cm}(0) = 0.023$, 2, and 4 km/s (corresponding to total translational energies of the cluster 2.6×10^{-2} (i.e., thermal impact energy), 193.3, and 773.25 eV, respectively). Collision with the highest velocity resulted in penetration of most of the cluster into the surface, sudden intense heating of the cluster (Figure 3c) accompanied by melting and disordering of the cluster and local melting of the surface, significant implantation and mixing, and severe damage to the cluster and substrate surface (in the form of crater formation); see Figure 4c. Collision with $V_c^{cm}(0) = 2$ km/s leads to partial penetration of the cluster into the surface followed by a recoil (see Figure 5), heating of the cluster to an internal temperature of ~1800 K (see Figure 3b), melting, less severe damage to the substrate surface, significant spreading of the cluster, and a certain degree of intermixing between the cluster and surface atoms; see

Figure 4b. Finally, in collision of the cluster with the lowest, thermal, velocity $V_c^{cm}(0) = 0.023$ km/s, the cluster accelerated toward the surface upon entering the attractive range of the interaction potential (see Figure 5b), and the internal temperature of the cluster did not exceed its melting temperature (estimated to be ~900 K; see section 3.3) during the collision (Figure 3a). This low-velocity collision did not damage the target surface. Moreover, the colliding cluster maintained a high degree of order as well as crystalline shape throughout the process, resulting in a three-dimensional crystalline nanostructure deposited on the surface; see Figure 4a.

3.2. Collisions with Adsorbed Liquid Films. We turn next to a discussion of the results of collisions of the cluster with adsorbed liquid films. Upon collisions of the incident cluster with the target surface its incidence translational motion is strongly attenuated (see Figures 6a and 7a for collisions with Ar and Xe films, respectively, and in each case for several incidence velocities $V_c^{cm}(0)$). The attenuation is accomplished by conversion of the cluster incidence kinetic energy (K_c^{cm}) into potential and kinetic energies of internal degrees of freedom of the cluster ($E_{k,c}^{int}$ and $E_{p,c}^{int}$) and those of the target.

For collisions in the energy range considered by us, the penetration depth of the incident cluster into the target fluid film shows some dependence on the substance of the fluid, and for the low-density film (Ar) the attenuation length shows a marked dependence on the incidence velocity (see Figure 6b). Thus for the Ar film the incidence translational energy of the cluster was dissipated within ~50 a_0 and ~100 a_0 for $V_c^{cm}(0) = 2$ and 4 km/s, respectively, while for the Xe film penetration depths of ~50 a_0 to 70 a_0 were found for incidence velocities between 1.5 and 4 km/s (see Figure 7b,b').

The variations versus time of the total internal energy of the cluster relative to its initial translational energy ($\delta E_T \equiv \Delta E_c^{int}(t)/K_c^{cm}(0)$) are shown in Figures 8a,b and 9a–d for collision processes of the cluster incident with various initial velocities onto adsorbed argon or xenon films, respectively. We note first the initial fast rate of variation of the internal energy of the cluster, reflecting efficient conversion of translational to vibrational energy for collisions with both target films. Furthermore, for both adsorbed films the fractional change in the cluster total internal energy δE_T, measured at the highest value (see Figures 8a,b and 9a–d), is approximately independent, for each film, of the incident velocities (the absolute magnitudes of ΔE_c^{int} are of course dependent on the initial translational energy of the cluster, $K_c^{cm}(0)$).

Comparison of the results shown in Figures 8 and 9 demonstrates that the rate of energy deposition into the cluster and in particular the branching ratio between the change in the internal total energy of the cluster, ΔE_c^{int}, and the energy dissipated into the fluid substrate depend strongly on the nature of the target surface. Overall, the internal total energy increase of the cluster incident onto the adsorbed xenon film is about twice that occurring for collision with the lower density adsorbed film (argon). The dependence of the energy branching ratio, δE_T, on materials' characteristic parameters, is discussed in section 4.

The partitioning of the energy deposited into the cluster between the potential ($\delta E_{p,c}^{int}$) and kinetic ($\delta E_{k,c}^{int}$) components (the latter shown also as the internal kinetic temperature, T_c^{int}), shown in Figures 8–10 for the Ar and Xe films, respectively, is reflected also in the state of the cluster subsequent to the collision with the fluid surface. Collisions of the cluster with an argon liquid surface are characterized by a relatively smaller energy flow into the cluster than in the higher-density xenon film case (compare Figures 8a,b and 9a–d), leading to fast heating to a maximum temperature of ~800 K for $V_c^{cm}(0) = 2$ km/s and ~1800 K for $V_c^{cm}(0) = 4$ km/s (see Figure 8c), which are much smaller than the internal temperatures achieved via collisions with the same velocities with the bare Cu(111) surface (see Figure 3b,c) or with the xenon film (see Figure 10). The heating rates for the two

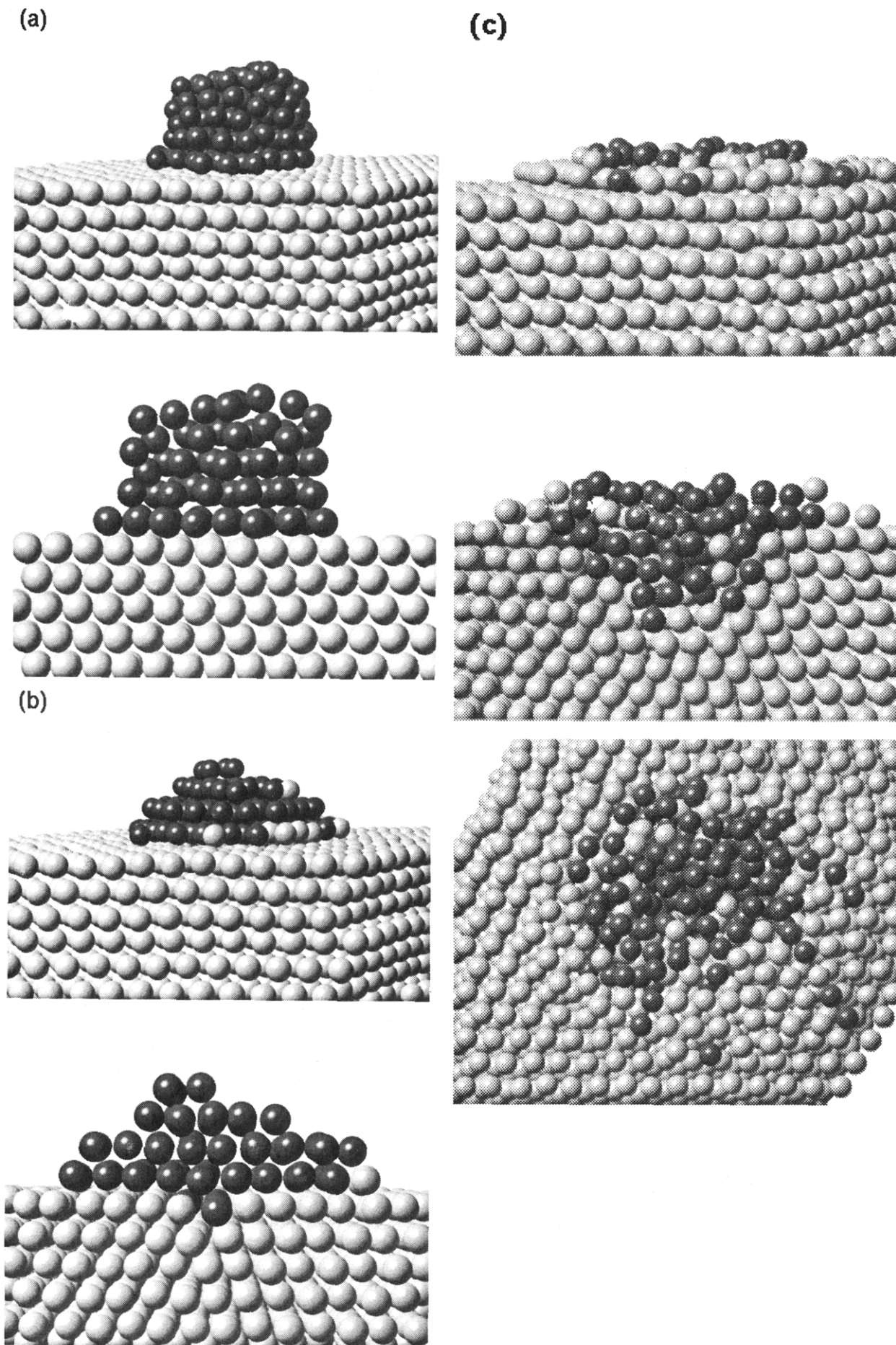**(a)**

(c)

(b)

Figure 4. Selected atomic configurations from simulations of collisions of an initially icosahedral Cu_{147} cluster with a Cu(111) surface. The configurations in (a)–(c) correspond to incident velocities of 0.023, 2, and 4 km/s, respectively. In each case the top figure gives a perspective view, and the one below is a cut through the middle of the system. The bottom panel in (c) is a view from above illustrating the spreading of the cluster for collision with the highest impact velocity. Light and dark balls represent surface and cluster atoms, respectively.
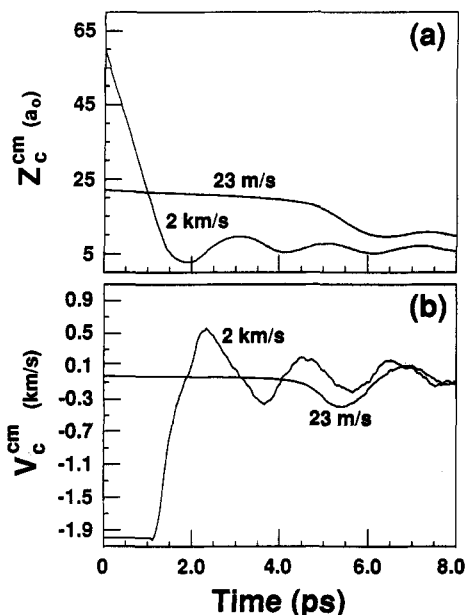
Figure 5. Variations of the position of the center of mass, Z_c^{cm}, and of the translational velocity, V_c^{cm}, of a Cu_{147} cluster colliding with a Cu(111) surface, plotted versus time for two incidence velocities, 23 m/s and 2 km/s. The average position of the topmost layer of the Cu(111) surface before the collision is at z = 0. The slow collision starts with Z_c^{cm} (t = 0) = 22 a_0 and the faster one with Z_c^{cm}(t = 0) = 60 a_0. Negative center of mass velocities correspond to motion toward the target Cu(111) surface. Note the acceleration of the translational motion of the slow cluster (23 m/s) as he enters the interaction range with the surface, and the abrupt stopping, followed by a recoil, of the motion of the cluster incident with V_c^{cm}(0) = 2 km/s. Center of mass distance in atomic units, velocity in km/s, and time in picoseconds.
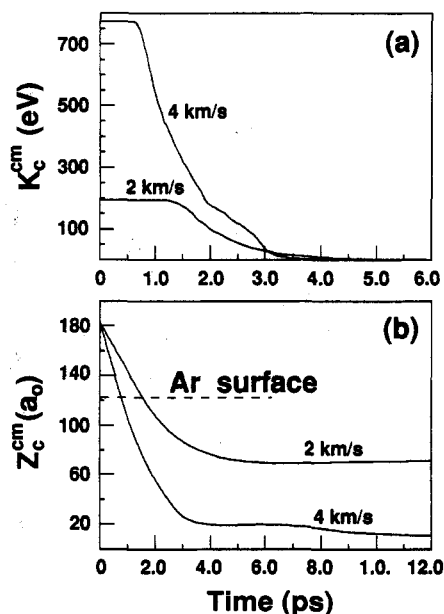

Figure 6. Translational kinetic energy (K_c^{cm}, in a) and center of mass position (Z_c^{cm}, in b) of a Cu_{147} nanocluster incident onto adsorbed liquid argon, plotted versus time. Results are shown for two incidence velocities, 2 and 4 km/s. The origin of the distance axis in (b) is at the average location of atoms in the topmost layer of the underlying crystalline Cu(111) substrate. The average location of the top of the adsorped liquid Ar films is indicated. Energies, distances, and times in units of electronvolts, Bohr radius (a_0), and picoseconds, respectively.

incidence collision velocities were $\sim$2.5 × 10^{14} and $\sim$10^{15} K/s for the low and high velocity, respectively. For the low-velocity collision the heated cluster, embedded in the hot argon liquid, did not undergo melting, maintaining to a large degree its original icosahedral order and shape (see Figure 11a). During subsequent evolution of the system cooling (at a rate of $\sim$4 × 10^{13} K/s)
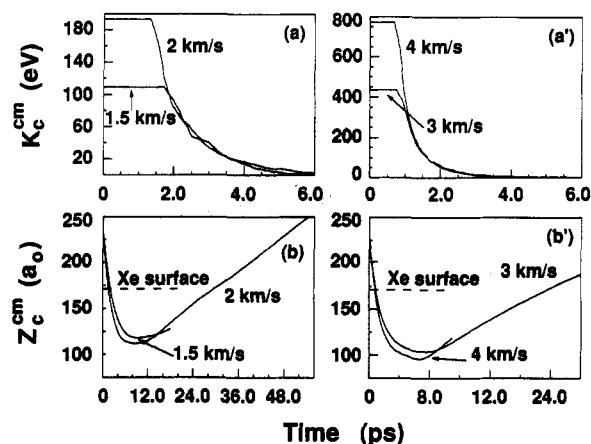

Figure 7. (a, a') Same as Figure 6a but for a Cu_{147} cluster colliding with a Xe liquid film. Results for incidence velocities of 1.5 and 2 km/s are shown in (a) and for 3 and 4 km/s in (a'). (b, b'): Same as Figure 6b but for a Cu_{147} colliding with a Xe liquid film.
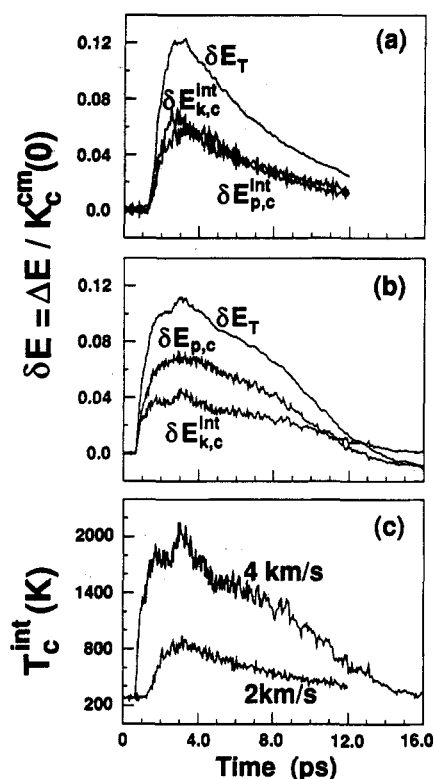

Figure 8. (a, b) Time evolutions of the changes in the internal total, kinetic and potential energies of a Cu_{147}, equilibrated initially at 300 K, during collisions with a 120 a_0 thick adsorbed Ar film for two incidence velocities; 2 km/s in (a), and 4 km/s in (b). The changes in the internal energies are scaled by the initial translational kinetic energy of the incident cluster, k_c^{cm}(0) (which equals 193.3 and 773.25 eV for the slow and high velocities, respectively) to form the branching ratios δE ≡ $\Delta E/K_c^{cm}$(0), with δE_T, $\delta E_{k,c}^{int}$ and $\delta E_{p,c}^{int}$ corresponding to the changes in the total internal energy of the cluster (ΔE_c^{int}), and in its internal kinetic ($\Delta E_{k,c}^{int}$) and potential ($\Delta E_{p,c}^{int}$) energies, respectively. (c) Time evolution of the internal temperature of the Cu_{147} cluster during collisions with an argon-covered Cu(111) surface. Note the changes at t $\sim$ 3 ps in the energies and internal temperature of the cluster incident with a velocity of 4 km/s, caused by its approach and landing on the underlying Cu(111) surface. Temperature in degrees kelvin and time in picoseconds.

occurred via heat transport in the fluid, dissipation into the substrate solid surface, and partial evaporation of the liquid. In the case of collision with V_c^{cm}(0) = 4 km/s the "heat-shocked" superheated cluster first melted and cooled to $\sim$1400 K at a rate of $\sim$2.5 × 10^{14} K/s. (Note the sudden increase in T_c^{int} at $\sim$2.5 ps, see Figure 8c, which may be associated with reflection of the impulse wave in the liquid from the underlying Cu(111) surface.) Subsequently the cluster continued its decelerated motion while
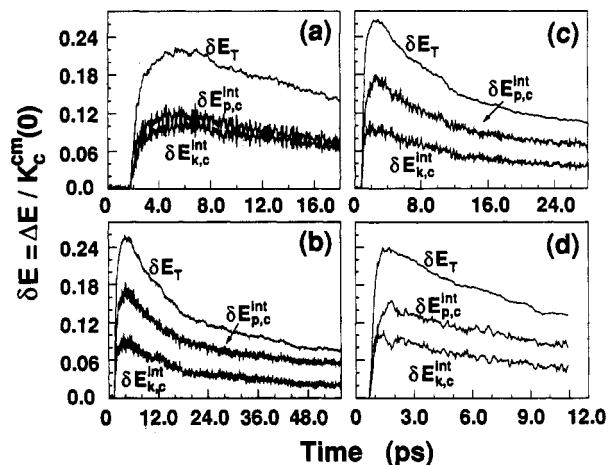
Figure 9. Same as Figure 8a,b, but for a Cu_{147} cluster incident into a xenon adsorbed film. Results are shown for incidence velocities of 1.5 (in a), 2 (in b), 3 (in c), and 4 km/s (in d).
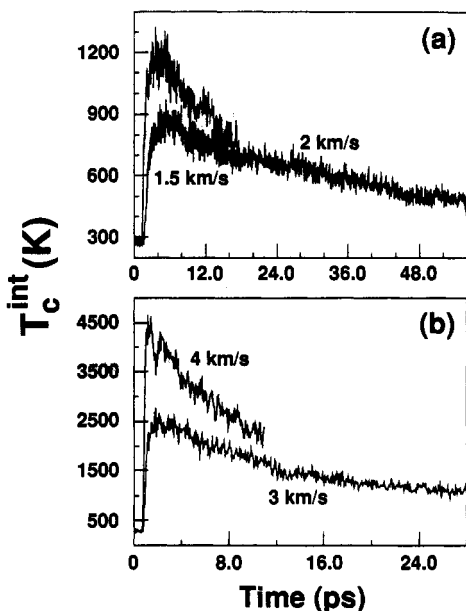

Figure 10. Time evolution of the internal temperature of a Cu_{147} cluster equilibrated initially at 300 K, during collisions with a xenon adsorbed film. Results are shwon for incidence velocities of 1.5 and 2 km/s in (a), and 3 and 4 km/s in (b). For the highest velocity results are shown only for the initial heating and cooling stages. For both collisions shown in (b) the cluster remains as a liquid hot droplet for over 100 ps, continuing to cool at a relatively slow rate.

continuing to cool, soft landed on the Cu(111) surface, and recrystallized into an ordered three-dimensional adsorbed nanostructure (see Figure 11b where results corresponding to two stages during the collision process are shown, one corresponding to the liquidlike state of the cluster and the other to a recrystallized state on top of the Cu(111) surface). Here, as well as in other cases, most of the excess rare-gas atoms may be desorbed by mild heating of the substrate at the end of the process, without altering in a substantial way the state of the deposited nanocluster.

As evident from Figure 10 incidence into the heavier mass adsorbed fluid (Xe) leads to ultrafast heating of the cluster with rates dependent on the incidence velocities (1.3 × 10^14, 2.5 × 10^14, 9 × 10^14, and 24 × 10^14 K/s for $V_c^{cm}(0)$ = 1.5, 2, 3, and 4 km/s, respectively, to maximum temperatures T_c^{int} ~ 900, 1150, 2500, and 4250 K). In all cases, except for $V_c^{cm}(0)$ = 1.5 km/s the cluster first superheated. Subsequent cooling of the cluster occured first at a fast rate (e.g., 0.4 × 10^14 K/s, from 1150 to 700 K in the time interval 6 ps ≲ t ≲ 18 ps for $V_c^{cm}(0)$ = 2 km/s; see Figure 10a), via melting of the cluster (consuming latent heat), and heat dissipation through the liquid. During this fast-cooling stage the thermally shocked melted cluster underwent

quenching to a lower temperature. If the temperature at the end of this cooling process is low enough (that is, below the "cluster glass transition temperature" (as in the case of collision of the cluster with the xenon film with $V_c^{cm}(0)$ = 2 km/s where the temperature at the end of the first fast quench was 700 K, that is, 200 K below the estimated melting temperature of the cluster; see section 3.3) the quenched cluster is arrested in a highly disordered glassy structure, confined, and frustrated by the presence of rare-gas atoms (see Figure 11c). The following cooling stage (e.g., $t \gtrsim 18$ ps for V_c^{cm} = 2 km/s; see Figure 10a) is characterized by a smaller cooling rate (~5.5 × 10^12 K/s), dominated by heat transport and evaporative processes of the fluid. For the higher incidence velocities, the temperature of the cluster after the initial ultrafast cooling stage (e.g., $t > 12$ ps for $V_c^{cm}(0)$ = 3 km/s; see Figure 10b) was much higher than its freezing (or melting) temperature, and the cluster remained in a hot-liquid state, cooling in the fluid at a relatively slow rate.

3.3. Glassy Cluster States. For the case of collision into a xenon film with $V_c^{cm}(0)$ = 2 km/s, the cluster remained, throughout the evolution of the system after the melting and quench stage, in a highly disordered state, characterized by a significant excess internal potential energy above that corresponding to the fully ordered ground state of the cluster. The initial sudden jump to high temperature coupled with the ultrafast cooling arrest the cluster in a configurationally disordered glassy state, preventing activated reordering and structural annealing of the cluster.[30]

Characterization and differentiation of the glassy state of matter from other disordered forms is a complex subject marred by some ambiguity. For our purpose we take as a glass the state of the material obtained via a sudden quench from a high-temperature melt. The "caloric history" of the Cu_{147} cluster incident into a xenon film at a velocity of 2 km/s is shown in Figure 12 (solid triangles and small dots corresponding to the initial heating during impact and subsequent cooling, respectively), together with the histories of other glass formation processes, and the "caloric curve" for an isolated Cu_{147} icosahedral cluster obtained via microcanonical equilibrium simulations (solid circles) exhibiting a characteristic melting curve for the cluster. As seen, collision of the cluster with the liquid first increases the internal kinetic and potential energies of the cluster (up arrow, solid triangles) following a trajectory which resembles that of the equilibrium heating process. Subsequent melting and energy-transfer processes to the surrounding fluid result in a quench (small dots, down arrow) into a state with an average internal potential energy of ~–445 eV and an internal kinetic energy of ~7 eV. The energy of the so obtained cluster cooled further to 0 K is shown by the empty equare. For comparison we show by a circle the low-potential energy state of the isolated crystalline icosahedral cluster, and by a star the energy of a glassy Cu_{147} isolated cluster, instantaneously quenched to 0 K from an initially equilibrated state at 1500 K, which we take to be the "ideal glassy" state of the cluster. Finally, the state obtained by heating the ideal glassy cluster to 350 K is denoted by the empty diamond (with a potential energy of ~–445 eV). As evident from these results, the glassy state produced by the collision process is of slightly lower potential energy (when cooled to 0 K) then the "ideal glass" obtained via an instantaneous quench of an isolated melted Cu_{147} cluster. However, when heating the latter to the temperature of the final state of the cluster quenched in xenon, their potential energies nearly coincide.

To further characterize energetically and structurally the states of the cluster we show in Figures 13 and 14, distributions of particles' potential energies and particle positions versus distance from the center of the cluster (R), and distributions of the potential energies of particles, for the clusters and states discussed in Figure 12. First, we note the smeared-out character of the positional and energy distributions for the quenched clusters as compared to those corresponding to the crystalline icosahedral cluster
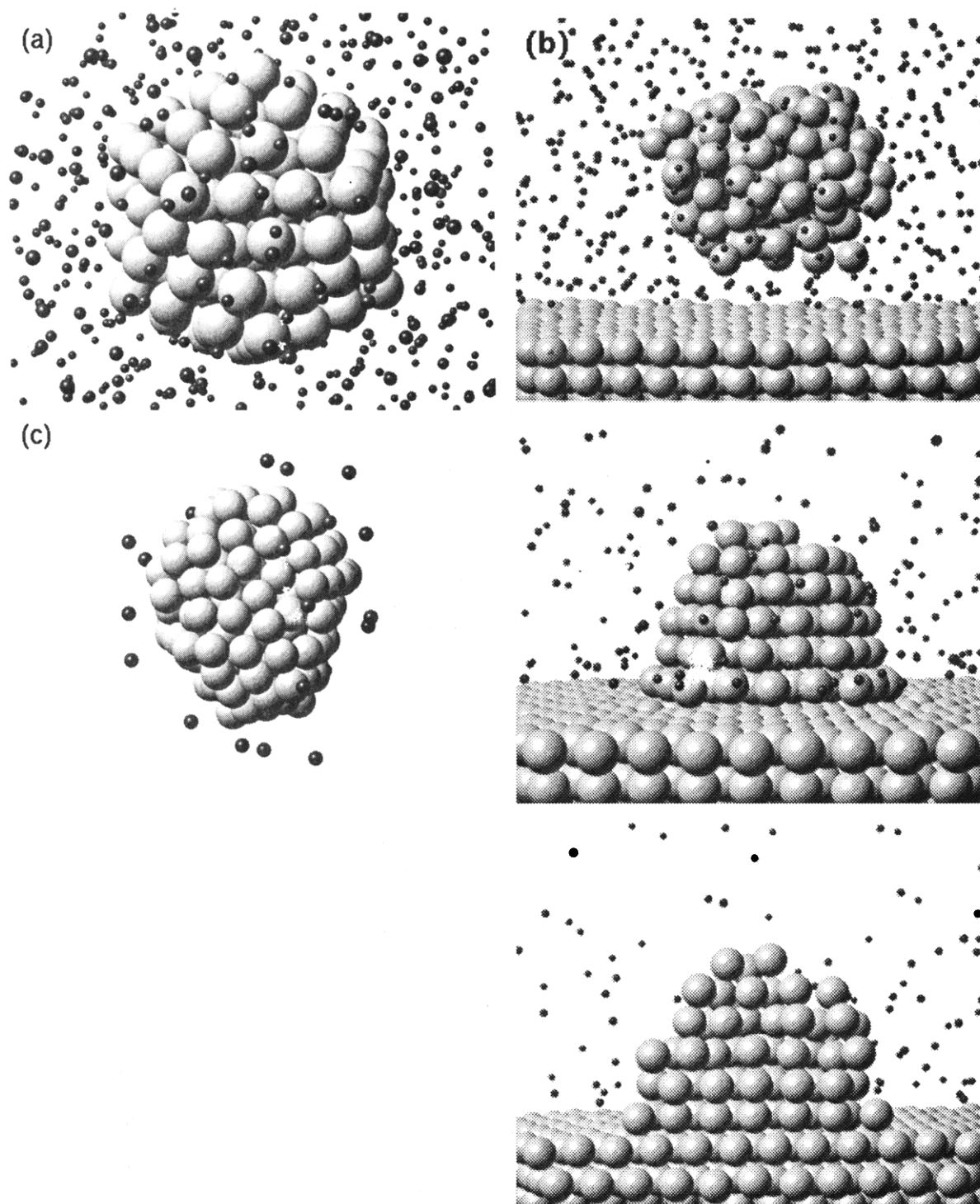
Figure 11. Selected atomic configurations from simulations of collisions of an initially icosahedral Cu_{147} cluster with liquid films adsorbed on a Cu(111) surface. Shown in (a) is the Cu_{147} 10 ps after collision with an incident velocity of 2 km/s into a liquid Ar adsorbed film. The cluster exhibits icosahedral symmetry. In (b) results are shown for the collision of the Cu_{147} with an incident velocity of 4 km/s into a liquid Ar film. The top panel illustrates the cluster in a melted state at $t = 4.5$ ps and the panel below shows the recrystallized nanostructure, at $t = 12$ ps, obtained after soft landing of the melted cluster on the Cu(111) surface. The bottom panel is a cut through the middle of the system shown in panel above it. Shown in (c) is a glassy Cu_{147} cluster obtained in a collision of the initially icosahedral cluster with an incident velocity of 2 km/s into a liquid Xe film. Larger balls represent copper atoms and small ones correspond to rare-gas atoms.

equilibrated at 350 K (Figure 13c). The distributions for the ideal Cu_{147} glassy state (Figure 13b) and that for the glassy cluster produced by the collision process (Figure 13a) are similar (with the former somewhat more uniformly distributed). Moreover, the similarity between the distributions for the two states is enhanced when comparing the reheated (to 350 K) ideal glassy cluster (Figure 14b) with that produced by the collision process (Figure 13a), or the quenched ideal glassy state at 0 K (Figure 13b) with the glassy collision product cooled further to 0 K (Figure 14a). The above analysis leads us to conclude that the glassy state of the cluster produced via energetic collision (with

$V_c^{cm}(0) = 2$ km/s) of a crystalline Cu_{147} nanocluster with a high-density liquid (Xe) is close structurally and energetically to the ideal glassy state obtained via an instantaneous quench from the melt.

4. Summary

The main results of our simulations of collisions of an icosahedral Cu_{147} cluster with argon and xenon liquid surfaces may be summarized as follows:

(i) Impact of the cluster onto a liquid results in conversion of the translation impact kinetic energy of the cluster to excitations
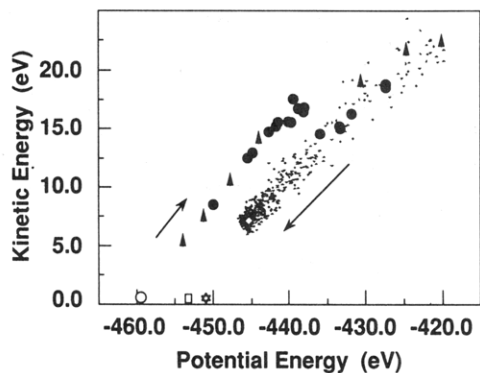
Figure 12. "Caloric histories" (internal kinetic energy versus potential energy) of Cu_{147} clusters. Filled circles correspond to equilibrium states of an isolated Cu_{147} cluster, obtained via microcanonical molecular dynamics simulations, exhibiting a characteristic "melting curve" for the cluster (data points in the melting, phase-coexistence region, i.e., about a kinetic energy of ~15 eV, i.e., ~900 K for the Cu_{147} cluster, where obtained for both heating and cooling of the cluster). The empty circle corresponds to an icosahedral isolated Cu_{147} cluster cooled to 0 K. States of a Cu_{147} cluster recorded during the fast heating process occurring at the initial stage of its collision, with an incident velocity of 2 km/s, into an adsorbed liquid film of xenon, are shown by large filled triangles. States of the colliding cluster recorded during its subsequent fast quench and cooling stages are shown by small dots. Note that during heating (particularly for internal kinetic energies less than 15 eV, that is below the equilibrium melting temperature of the cluster) the states of the colliding cluster follow rather closely those of the equilibrium isolated cluster). States at the end of the collision cooling process (downward arrow) correspond to a glassy state of the cluster. The energy of this glassy collision product further cooled to 0 K, is denoted by an empty square. The energy of the "ideal glass" state of an isolated Cu_{147} cluster, obtained via an instantaneous quench from a melt at 1500 K is denoted by a six-sided star. The energy of the "ideal glass" isolated cluster, reheated to 350 K is denoted by an empty diamond (coordinates ~7 and −445 eV) and is seen to coincide with that of the collision glassy cluster. Energies in electrovolts.
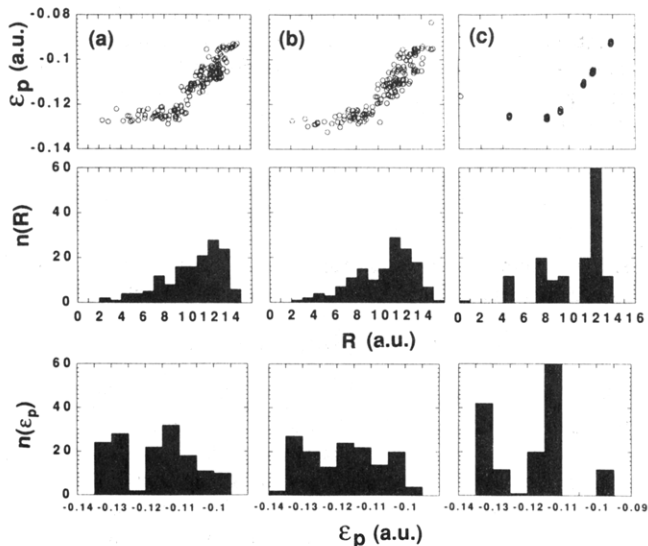

Figure 13. Distributions of particle potential energies, ϵ_p, (top panel) and particle positions ($n(R)$, middle panel), plotted versus radial distance (R) from the center of the cluster. In the bottom panel distributions of particle potential energies $n(\epsilon_p)$ in the clusters plotted versus ϵ_p, are shown. Results are shown in column (a) for a glassy state of a Cu_{147} cluster at a final temperature of 350 K, obtained via collision with an incident velocity of 2 km/s with a xenon adsorbed liquid film. The results in column (b) were obtained for an isolated Cu_{147} cluster quenched instantaneously to 0 K from a melt at 1500 K (the same results were obtained for a Cu_{147} cluster quenched from a melt at 1200 K). Distributions for an isolated icosahedral Cu_{147} cluster equilibrated at 350 K are shown in column (c). Energies and distances in atomic units.

of the internal degrees of freedom of the cluster and the liquid and initiation of an impulse shock-wave in the liquid, leading to attenuation of the translational motion of the cluster. For
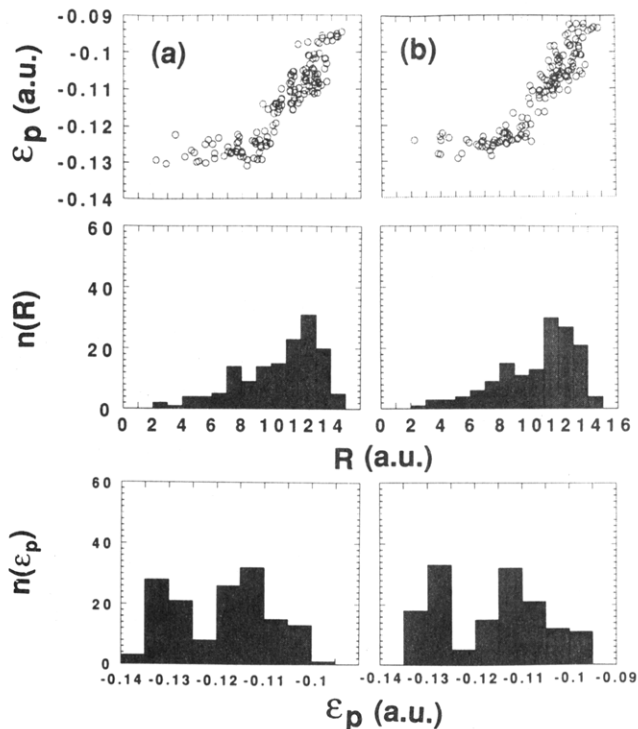

Figure 14. Distributions of particle potential energies, ϵ_p, (top panel) and particle positions, $n(R)$ (middle panel), plotted versus radial distance (R) from the center of the cluster. Distributions of particles potential energies, $n(\epsilon_p)$, plotted versus ϵ_p are given in the bottom panel. Results in column (a) are shown for the glassy state obtained via collision of a Cu_{147} cluster incident with a velocity of 2 km/s into a liquid xenon film (see column (a) in Figure 13), cooled to 0 K. The results shown in column (b) were obtained by reheating to 350 K of the instantaneously quenched "ideal glass" Cu_{147} cluster (see column (b) in Figure 13). Energies and distances in atomic units.

incidence velocities, $V_c^{cm}(0)$, in the range 1.5–4 km/s (that is impact energies, $K_c^{cm}(0)$, in the range 110–775 eV) the attenuation lengths in Ar are between 50 a_0 and 100 a_0 and in Xe between 50 a_0 and 70 a_0.

(ii) The branching ratio associated with internal total energy increase of the cluster, $\delta E_T = \Delta E_c^{int}/K_c^{cm}(0)$, is $\simeq 0.12$ for collisions with Ar with incidence velocities in the range 2 km/s $\leq V_c^{cm}(0) \leq 4$ km/s, and $\simeq 0.24$ for collisions with xenon for incidence velocities in the range 1.5 km/s $\leq V_c^{cm}(0) \leq 4$ km/s.

(iii) Conversion of the cluster impact translational kinetic energy into internal degrees of freedom of the cluster during attenuation of its motion results in ultrafast heating of the cluster with rates in the range 10^{14}–10^{15} K/s. Depending on the cluster incidence velocity and on the material of the fluid target, this thermal shock (temperature jump) can lead to superheating and subsequent melting of the cluster (the melting temperature of the cluster is estimated to be $T_c^m \sim 900$ K; see Figure 12).

(iv) Following the initial heating stage the internal temperature of the cluster decreases with initial cooling rates as high as ~10^{14} K/s. The cooling process occurs via heat transport in the liquid, dissipation in the underlying solid substrate, and evaporation. Cooling rates of the cluster in the first stage are higher for collisions leading to melting of the cluster due to consumption of the latent heat of melting.

(v) In collisions of the cluster with a 120 a_0 thick argon film adsorbed on a Cu(111) surface with an incident velocity of 2 km/s the cluster did not melt and remained ordered throughout the process, while for $V_c^{cm}(0) = 4$ km/s the cluster first superheated and melted and subsquently soft landed and recrystallized on the underlying substrate forming a three-dimensional adsorbed structure.

(vi) Collisions of the cluster with $V_c^{cm}(0) = 1.5$ km/s with a

170 a_0 thick adsorbed xenon film did not lead to melting, while for collisions with $V_c^{cm}(0) \geq 2$ km/s superheating and melting occurred.

(vii) For a certain range of incidence velocities, depending on the projectile and target materials (and in general on the size of the incident cluster, i.e., $V_c^{cm}(0) \simeq 2$ km/s, that is a translation energy of $\sim$200 eV, for a Cu_{147} cluster impinging into xenon) ultrafast cooling of the superheated cluster during the melting process (consuming latent heat of melting), accompanied by rapid heat dissipation to the liquid, quenches the cluster to a sufficiently low temperature such that it is arrested in a glassy state. From the caloric curve for the Cu_{147} cluster (Figure 12) we estimate the melting temperature of the cluster to be $T_c^m \sim 900$ K, whereas the bulk melting temperature of copper was determined[18] from MD simulations using the same EAM potentials to be $T_b^m = 1285 \pm 10$ K. Therefore, glassification of the copper cluster occurs when a fast quench ($\sim 10^{14}$ K/s) of the heat-shocked cluster cools it to a temperature about 200 K below its melting point (see Figure 10a where the internal temperature of the cluster, colliding with a Xe film with an incident velocity of 2 km/s, was 700 K at the end of the initial fast cooling stage, resulting in a glassy state). In this context we note that while elemental metals are characterized by low "glass formability",[12-14] it has been shown experimentally and discussed theoretically that the propensity to form metallic glasses is dramatically enhanced for finite liquid metal drops.[12]

In cases where the cluster internal temperature reaches above T_c^m and the temperature at the end of the initial fast cooling phase is not low enough (i.e., above T_c^m or close to it) the cluster remains in a hot liquid–droplet state for a prolong period (simulations for clusters incident with $V_c^{cm}(0) \geq 3$ km/s into xenon, carried for over 100 ps, resulted in liquid droplets), which may eventually cool, via collisions with the surrounding atoms, and recrystallize (in our simulations this did not occur since the liquid evaporates and the cooling rates become exceedingly slow).

From our present and previous[7] simulations of collisions between nanoclusters and liquid targets we observed that the energy redistribution and partitioning pathways and the final states that are achieved in such collision processes depend, for given collision conditions (such as the incident energy), on the materials properties of the collision partners (that is, incident cluster and target liquid). Of particular interest are our observations pertaining to the branching ratio δE_T, relating the increase of the internal total energy of the cluster to the incidence translational kinetic energy of the projectile cluster (see ii above). Our simulations of collisions of sodium chloride[7] and copper nanoclusters with rare-gas liquids showed that, for a given material of the cluster, δE_T can be varied by selecting the material of the target fluid. Furthermore, we found that for a given cluster δE_T is rather insensitive to the cluster incidence velocity (i.e., impact translational energy), at least in the range which we investigated (see Figure 8a,b for incidence of Cu_{147} into Ar with $V_c^{cm}(0) = 2$ and 4 km/s where $\delta E_T \simeq 0.10$–0.12 and Figure 9 for incidence into Xe with 1.5 km/s $\leq V_c^{cm}(0) \leq 4$ km/s, where $\delta E_T \simeq 0.20$–0.24). In the following we present a simple model which correlates the above observations with characteristic materials properties of the collision partners and can be used as a guide for controlling the consequences of the collision process via proper selection of the cluster and fluid target materials.[31]

Consider a deformable projectile of mass M_p shaped as a finite rectangular slab with cross sectional area A and height L, made of a material with mass density ρ_p and sound velocity s_p, impacting with a velocity v_{0p}, directed along the normal z direction, a deformable target at rest. The surface of the target lies in the (xy) plane, and the material of the target is characterized by a mass density ρ_t and sound velocity s_t (the target may be taken as a thick adsorbed fluid film or as a macroscopically large body).

Assuming that in the initial stage of the collision mass displacements and stress impulses occur only along the z direction,

the collision will set a stress pulse in the target, $-\sigma$, traveling along the normal direction in the fluid with a velocity s_t (the analysis can be easily generalized to supersonic pulse propagation by defining a velocity of propagation $c_t = \mathcal{M}_t s_t$, where $\mathcal{M}_t$ is the Mach number). In a time interval $d\tau$ the wave front of the stress pulse moves a distance $dz = s_t\, d\tau$ and an element of mass $\rho_t A\, dz$ in the fluid acquires a velocity v. The momentum equation for the element is[32]

$$-\sigma A\, d\tau = (\rho_t A\, dz)v = \rho_t A s_t v\, d\tau \quad (3)$$

and thus

$$\sigma = -\rho_t s_t v \quad (4)$$

Note that immediately after impact the material of the target within the impact area (A) acquires the velocity of the incident projectile, v_{0p}, and thus the initial compressive stress in the target is given by

$$\sigma_0 = -\rho_t s_t v_{0p} \quad (5)$$

The compressive stress in the target at the interface with the projectile acts on the projectile (action–reaction) performing on it work of deformation, (which we take as a compression of the height of the rectangularally shaped projectile by dl; extension to include sideways expansion in the xy directions can be incorporated using the Poisson ratio of the material):

$$dw = \sigma A\, dl = \rho_t s_t v(\tau) A\, dl \quad (6)$$

The decelerated translational velocity of the projectile at time τ is given by $v(\tau) = v_{0p} - a\tau$, where we assume a constant deceleration (whose magnitude can be obtained from eq 5). The strain in the projectile due to the stress-induced deformation is $\epsilon_p = \sigma/Y_p = dl/dz_p$, where Y_p is the Young modulus of the projectile, and $dz_p = s_p\, d\tau$ (here too the velocity of propagation of the stress impulse in the projectile could be taken as $c_p = \mathcal{M}_p s_p$, where $\mathcal{M}_p$ is a Mach number). Consequently the amount of compression can be written as $dl = \sigma s_p\, d\tau/Y_p$, and the work performed on the projectile during the time τ_0, measured from the moment of initial contact, is given by

$$W = \int_0^{\tau_0} dw = \frac{\rho_t^2 s_t^2 s_p A}{Y_p} \int_0^{\tau_0} (v_{0p} - a\tau)^2\, d\tau \quad (7)$$

After integration we obtain for W, which is also the amount of increase of the total internal energy of the projectile, ΔE^{int}:

$$\Delta E^{int} = \alpha \rho_t^2 s_t^2 s_p A v_{0p}^2 \tau_0 / Y_p \quad (8)$$

where $\alpha = 1 - (\Delta v_p/v_{0p}) + {}^1/_3(\Delta v_p/v_{0p})^2 < 1$, and $\Delta v_p = a\tau_0$ is the change in the projectile's translational velocity occurring in the time interval τ_0. For definiteness we take τ_0 to be of the order of L/s_p, that is the time it takes a stress impulse moving with sound velocity s_p to traverse the linear dimension of the projectile (for longer times reflection of the stress wave from the boundary surface of the projectile has to be considered). With this choice for τ_0 we obtain for the projectile internal energy branching ratio, $\delta E^{int} = \Delta E^{int}/{}^1/_2 M_p v_{0p}^2$:

$$\delta E^{int} = \alpha'(\rho_t^2 s_t^2/\rho_p Y_p) = \alpha'(\rho_t s_t/\rho_p s_p)^2 \quad (9)$$

where we have used the relation $s_p = (Y_p/\rho_p)^{1/2}$, and $\alpha' = 2\alpha$.

The above simple model and the expression for the branching ratio δE^{int} (eq 9) emphasize that energy conversion and redistribution in collisions between condensed phase projectiles (such as a nanoscale, or larger, clusters) and condensed phase targets (such as fluids) are related to condensed-phase materials properties of the collision partners. The above relations may be used to guid the choice of collision partners in order to control the redistribution of the impact translational energy. For example, from eq 9 we

obtain that the internal energy branching ratios for collisions of a given projectile and incidence velocity with two different materials targets, are related by (assuming α' in eq 9 to be a constant):

$$\delta E_1^{int}/\delta E_2^{int} \sim (\rho_{t1} s_{t1}/\rho_{t2} s_{t2})^2 \qquad (10)$$

For the liquid targets investigated by us here (Ar and Xe with[33] $\rho_{Ar} = 1.41$ g/cm^3, $\rho_{Xe} = 3.0$ g/cm^3, $s_{Ar} = 974$ m/s, and $s_{Xe} = 645$ m/s), eq 10 yields the ratio $\delta E_{Xe}^{int}/\delta E_{Ar}^{int} \approx 2.5$ which is in good correspondence with the results of our simulations yielding $\delta E_T(Xe)/\delta E_T(Ar) \gtrsim 2.2$ (see Figure 8 and 9) for incidence velocities in the range 2.0–4.0 km/s.

These results suggest a new controlled growth method of nanophase materials based on epitaxial deposition of clusters, prepared and mass-selected in the gas phase, onto adsorbed liquid films. In addition, the method could allow controlled preparation of well-characterized samples for investigations of surface supported clusters using tip-based (scanning tunneling and atomic force) microscopies, as well as isolation of clusters in solid inert matrices. As shown above, the nature of the deposited nanoscale growth units (shape, as well as crystalline versus glassy structures) may be controlled via appropriate selection of the target liquid film and incidence translational energy of the clusters. While in our investigations rare-gas fluid targets were used, one may wish to explore polyatomic fluids as substrates, where excitations of internal vibrations, in addition to translational degrees of freedom, may provide efficient energy-transfer channels.

Finally, the ultrafast heating and particularly cooling rates (in excess of 10^{14} K/s) of finite aggregates which may be achieved by high-velocity collisions of clusters with liquids exceed the record laboratory rates reported to date. Consequently the methods suggested by our theoretical investigation may open new experimental avenues for ultrafast heat processing and for preparation and exploration of nanoglass materials aggregates.

References and Notes

(1) *Interfaces and Contacts*; Ludeke, R., Rose, K., Eds.; North-Holland: New York, 1983. *Thin Films and Interfaces*; Ho, P. S., Tu, K. N., Eds.; North-Holland: New York, 1982. *Epitaxial Growth*; Matthews, J. W., Ed.; Academic Press: New York, 1975. See reviews in *Mater. Res. Soc. Bull.* **1988**, *13*, 18.

(2) Yamada, I.; Takoska, G. H.; Usui, H.; Takagi, T. *J. Vac. Sci. Technol.* **1986**, *A4*, 722. Yamada, I. *Appl. Surf. Sci.* **1989**, *43*, 23. Takugi, T. *Ionized-Cluster Beam Deposition and Epitaxy*; Noyes: Park Ridge, NJ, 1988. Haberland, H.; Karrais, M.; Mall, M. *Z. Phys. D* **1991**, *20*, 413. Weaver, J. H.; Waddill, G. D. *Science* **1991**, *251*, 1444.

(3) See reviews by: (a) Gleiter, H. *Nanostruct. Mater.* **1992**, *1*, 1 and references therein. (b) Siegel, R. W.; Huggins, R. A.; Giordmaine, J. A.; Wachtman, J. B., Jr.; *Annu. Rev. Mater. Sci.* **1991**, *21*, 559. Siegel, R. W.; *Mater. Sci. Eng.* **1993**, B *19*, 37.

(4) Brice, J. C.; *The Growth of Crystals from Liquids*; North-Holland: Amsterdam, 1973. For molecular dynamics simulations of liquid-phase epitaxy see: Landman, U.; Cleveland, C. L.; Brown, C. S. *Phys. Rev. Lett.* **1980**, *45*, 2032. Landman, U.; Luedtke, W. D.; Ribarsky, M. W.; Barnett, R. N.; Cleveland, C. L. *Phys. Rev. B* **1988**, *37*, 4637, 4647.

(5) See review by: Landman, U.; Luedtke, W. D. In *Atomically Controlled Surfaces and Interfaces*, Tsukada, M., Kawazu, A., Eds.; *Appl. Surf. Sci.* **1992**, *60/61*, 1, and other articles therein.

(6) Sattler, K. In *Physics and Chemistry of Finite Systems*; Jena, P., Khanna, S. N., Rao, B. K., Eds.; Kluwer: Dordrecht, 1992; Vol. 1, p 61.

(7) Cheng, H.-P.; Landman, U. *Science* **1993**, *260*, 1304.

(8) For recent simulations of the dynamics of energetic collisions between atomic clusters and solid surfaces see: Cleveland, C. L.; Landman, U. *Science*

1992, *257*, 355 and references therein. Yamamura, Y.; Yamada, I.; Takagi, T. *Nucl. Instrum. Methods Phys. Res. B* **1989**, *37/38*, 902. Yamamura, Y. *Ibid.* **1990**, *45*, 707. Shapiro, M. H.; Tombrello, T. A. *Phys. Rev. Lett.* **1992**, *68*, 1613. Muller, K. H. *J. Appl. Phys.* **1987**, *61*, 2516. Hsieh, H.; Averback, R. S. *Phys. Rev. B* **1990**, *42*, 5365. Biswas, R.; Grest; G. S.; Soukoulis, C. M. *Ibid.* **1987**, *36*, 6434. Xu, G.-Q.; Holland, R. J.; Bernasek, S. L.; Tully, J. C. *J. Chem. Phys.* **1989**, *90*, 3831; *Ibid.* **1988**, *88*, 3376. Even, U.; Schek, I.; Jortner, J. *Chem. Phys. Lett.* **1993**, *202*, 303.

(9) For recent experiments of molecular beam scattering of rare-gase atoms from liquid surfaces see: Saecker, M. E.; Govoni, S.; Kowalski, D.; King, M. E.; Nathanson, G. M. *Science* **1991**, *252*, 1421.

(10) For experiments of collisions of clusters with solid targets see: Even, U; de Lange, P.; Jonkman, H.; Kommandeur, J. *Phys. Rev. Lett.* **1966**, *56*. Buehler, R. J.; Friedlander, G.; Friedman, L. *Ibid.* **1989**, *63*, 1292. Buehler, R. J.; Chu, Y. Y.; Friedlander, G.; Friedman, L. Kinnman, W. *J. Phys. Chem.* **1990**, *24*, 7665. Beck, R. D.; St. John, P. Homer, M. L.; Whetten, R. L. *Science*, **1991**, *253*, 879. *Chem. Phys. Lett.* **1991**, *187*, 122. St. John, P.; Beck, R. D.; Whetten, R. L. *Phys. Rev. Lett.* **1992**, *69*, 1467. Harbich, W.; Fedrigo, S.; Meyer, F.; Lindsay, D. M.; Lignieres, J.; Rivoal, J. C.; Kreisle, K. *J. Chem. Phys.* **1990**, *93*, 8535.

(11) (a) Suslick, K. *Science* **1990**, *247*, 1439. (b) Baikov, A. P.; Ivanchenko, B. A.; Motorin, V. I.; Musher, S. L.; and Shester, A. F. *Phys. Lett.* **1985**, *113A*, 38. Lin, C. J.; Spaepen, F.; and Turnbull, D. *J. Non-Cryst. Solids*, **1984**, *61/62*, 767. Mazzoldi, P.; Della Mea, G.; Battaglin, G.; Miotello, A.; Servidori, M.; Bacci, D.; and Jannitti, E. *Phys. Rev. Lett.* **1980**, *44*, 88. Davis, H. A. and Hull, G. B. *J. Mater. Sci.* **1987**, *11*, 215.

(12) Turnbull, D. *Contemp. Phys.* **1969**, *10*, 473.

(13) Chen, H. S.; Jackson, K. A. In *Treatise on Materials Science and Technology*; Herman, H., Ed.; Academic: New York, 1981; Vol. 20, p 215.

(14) Kelton, K. F. In *Solid State Physics*; Ehrenreich, H., Turnbull, D., Eds.; Academic: New York, 1991; Vol. 45, p 75.

(15) Allen, M. P.; Tildesley, D. J. *Computer Simulations of Liquids*; Clarendon: Oxford, 1987.

(16) Landman, U.; Barnett, R. N.; Luedtke, W. D. *Philos. Trans. R. Soc. London, A* **1992**, *341*, 337 and other articles therein. *Simulations of Liquids and Solids*; Ciecotti, G., Frenkel, D., McDonald, I. R., Eds.; North-Holland: Amsterdam, 1987.

(17) Daw, M. S.; Baskes, M. I. *Phys. Rev. B* **1984**, *29*, 6443. The parametrization which we use is after: Adams, J. B., Foiles, S. M.; Wolfer, W. G. *J. Mater. Res.* **1989**, *4*, 102.

(18) Barnett, R. N.; Landman, U. *Phys. Rev. B* **1991**, *44*, 3226.

(19) Maitland, G. C.; Rigby, M.; Smith, E. B.; Wakeman, W. A. *Intermolecular Forces*; Clarendon Press: Oxford, 1981.

(20) Landman, U.; Kleiman, G. G. In *Surface and Defect Properties of Solids*; The Chemical Society: London, 1977, Vol. 6, p 1.

(21) Zaremba, E.; Kohn, W. *Phys. Rev. B* **1977**, *15*, 1769; *Ibid. Phys. Rev. B* **1976**, *13*, 2270.

(22) For a compilation of results pertaining to rare-gas interaction with solid surfaces see: Vidali, G; Kim, G. Ihm. H.-Y.; Cole, M. W. *Surf. Sci. Rep.* **1991**, *12*, 133.

(23) Tang, K. T.; Toennies, J. P. *J. Chem. Phys.* **1984**, *80*, 3726.

(24) Chizmeshya, A.; Zaremba, E. *Surf. Sci.* **1989**, *220*, 443.

(25) Barker, J. A.; Rettner, C. T. *J. Chem. Phys.* **1992**, *97*, 5844 and references therein.

(26) Tully, J. C. *Surf. Sci.* **1981**, *226*, 461. Arumainayagam, C. R.; Madix, R. J.; McMaster, M. C.; Suzawa, V. M.; Tully, J. C. *Surf. Sci.* **1990**, *226*, 180.

(27) Baerends, E. J.; Ellis, D. E.; Ros, P. *Chem. Phys.* **1973**, *2*, 41. Delley, B.; Ellis, D. E.; Freeman, A. J.; Barenends, E. J.; Post, D. *Phys. Rev. B.* **1983**, *27*, 2132. Cheng, H.-P.; Ellis, D. E. *J. Chem. Phys.* **1991**, *94*, 3735.

(28) Fox, J. R.; Andersen, H. C. *J. Phys. Chem.* **1989**, *88*, 4019.

(29) Cleveland, C. L.; Landman, U. *J. Chem. Phys.* **1991**, *94*, 7376.

(30) The dependence of the probability of occurrence of amorphous and/ or glassy structures of clusters on the initial temperature and quench rate has been noted in a recent computer simulation study (Rose, J. P.; Berry, R. S. *J. Chem. Phys.* **1993**, *98*, 3262). Furthermore the inhibition of transformations of high-energy structural isomers to the ground-state structure at temperatures below a characteristic transition temperature has been discussed in the context of reactive cluster collisions. Kaukonen, H.-P.; Landman, U.; Cleveland, C. L. *J. Chem. Phys.* **1991**, *95*, 4997.

(31) The dependence of the energy-transfer efficiency on the effective mass ratio between the collision partners studied in the context of atom-surface collisions and accomodation, within the framework of binary collisions, is not applicable in our case. See: Goodman, F. O; Wachman, H. *Dynamics of Gas Surface Scattering*; Academic Press: New York, 1976. Amirav, A.; Cardillo, M. J.; Trevor, P. L.; Lim, C.; Tully, J. C. *J. Chem. Phys.* **1987**, *87*, 1796. Cohen, S. R.; Naaman, R.; Sagiv, J. *Phys. Rev. Lett.* **1987**, *58*, 1208. See also ref 9.

(32) Johnson, K. L. *Contact Mechanics*; Cambridge University Press: Cambridge, 1985; Chapter 11.

(33) *Argon, Helium and the Rare Gases*; Cook, G. A., Ed.; Interscience Publishers: New York, 1961; Vol 1, Thermophysical *Properties of Neon, Argon, Krypton and Xenon*; Rabinovich, V. A., Vasserman, A. A., Nedostup, V. I., Veksler, L. S., Eds.; Hemisphere Publishing: New York 1986. Aziz, R.; Bowman, D.; Lim, C. *Can. J. Chem.* **1967**, *45*, 2079.